

Loopy Cuts: Surface-Field Aware Block Decomposition for Hex-Meshing

MARCO LIVESU*, CNR IMATI, Italy

NICO PIETRONI*, University of Technology Sydney, Australia

ENRICO PUPPO, University of Genoa, Italy

ALLA SHEFFER, University of British Columbia, Canada

PAOLO CIGNONI, CNR ISTI, Italy

*: joint first authors

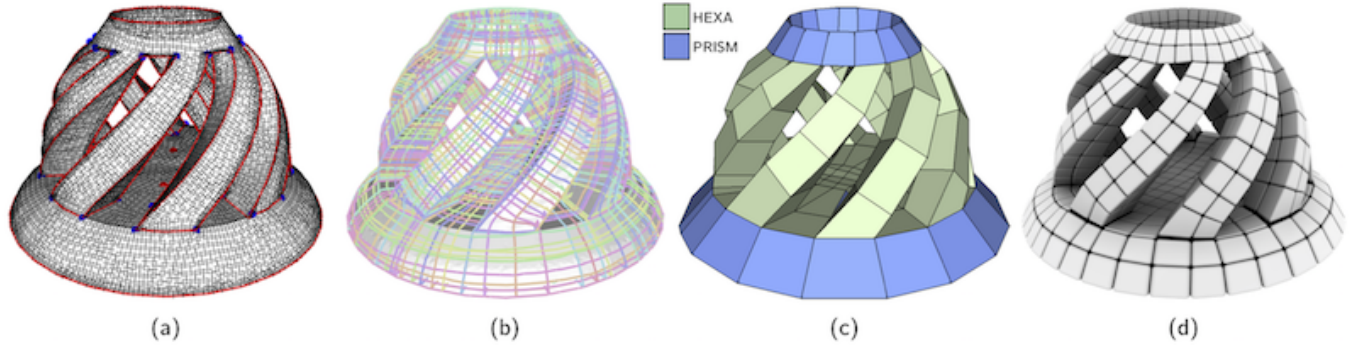


Fig. 1. We take as input a surface mesh together with a set of feature curves and a smooth surface field that aligns to them (a); we generate a pool of field-aware loops over it (b); and decompose the model into blocks by cutting it using surfaces bounded by algorithmically selected loops (c); we produce a hexahedral mesh from this block decomposition via midpoint subdivision and mesh optimization (d).

We present a new fully automatic block-decomposition hexahedral meshing algorithm capable of producing high quality meshes that strictly preserve feature curve networks on the input surface and align with an input surface cross-field. We produce all-hex meshes on the vast majority of inputs, and introduce localized non-hex elements only when the surface feature network necessitates those. The input to our framework is a closed surface with a collection of geometric or user-demarcated feature curves and a feature-aligned surface cross-field. Its output is a compact set of blocks whose edges interpolate these features and are loosely aligned with this cross-field. We obtain this block decomposition by cutting the input model using a collection of simple cutting surfaces bounded by closed surface loops. The set of cutting loops spans the input feature curves, ensuring feature preservation, and is obtained using a field-space sampling process. The computed loops are uniformly distributed across the surface, cross orthogonally, and are loosely aligned with the cross-field directions, inducing the desired block decomposition. We validate our method by applying it to a large range of complex inputs and comparing our results to those produced by state-of-the-art alternatives. Contrary to prior approaches, our framework consistently produces high-quality field aligned meshes while strictly preserving geometric or user-specified surface features.

Authors' addresses: Marco Livesu*, CNR IMATI, Genoa, Italy, marco.livesu@gmail.com; Nico Pietroni*, University of Technology Sydney, Sydney, Australia; Enrico Puppo, University of Genoa, Genoa, Italy; Alla Sheffer, University of British Columbia, Vancouver, Canada; Paolo Cignoni, CNR ISTI, Pisa, Italy
*: joint first authors.

© 2019 Association for Computing Machinery.
This is the author's version of the work. It is posted here for your personal use. Not for redistribution. The definitive Version of Record was published in *ACM Transactions on Graphics*, <https://doi.org/10.1145/nnnnnnn.nnnnnnn>.

CCS Concepts: • **Computing methodologies** → **Mesh models**; **Mesh geometry models**; **Volumetric models**; *Shape analysis*.

ACM Reference Format:

Marco Livesu*, Nico Pietroni*, Enrico Puppo, Alla Sheffer, and Paolo Cignoni. 2019. Loopy Cuts: Surface-Field Aware Block Decomposition for Hex-Meshing. *ACM Trans. Graph.* 1, 1 (June 2019), 16 pages. <https://doi.org/10.1145/nnnnnnn.nnnnnnn>

1 INTRODUCTION

Hexahedral and hex-dominant volumetric meshing of 3D shapes is a well investigated yet still open research topic. At their core, hexahedral meshing algorithms balance fidelity to the input surface geometry against element quality, and seek to compute meshes with well shaped, or as cuboid as possible, elements whose outer surface closely aligns with that of the input model (Section 2). To achieve high surface fidelity and to keep the element budget low, users prefer meshes whose external quads align with the surface curvature directions. Users also often strongly prefer meshes whose edges interpolate geometric or semantic surface feature curves. We propose *Loopy Cuts*, a robust new meshing algorithm that is specifically designed to satisfy these preferences.

Current attempts at automatic hex mesh generation fail to provide the combination of robustness, feature and curvature alignment we seek (Section 2). Methods based on adaptive grids [Maréchal 2009] or PolyCube maps [Livesu et al. 2013] do not effectively handle surface features that do not align with the global frame, and cannot easily support alignment to a curvature field (Figure 2). Methods that align mesh elements with a volumetric frame field generate

meshes that support feature and field alignment [Li et al. 2012; Liu et al. 2018] but lack robustness, failing to automatically mesh more complex inputs (Section 6, Figure 3).

Our method complements these existing approaches by providing the desired combination of alignment and robustness. It achieves this goal by employing a meshing strategy that mimics semi-manual block decomposition. While this popular semi-manual approach is commonly used in industry to create quality hex meshes, existing attempts to replicate the process automatically have failed to produce similar quality results. We successfully automate this process, producing results on-par with those obtained using manual decomposition on a wide range of inputs. Our method produces all-hex meshes on the vast majority of inputs (Figure 13), and introduces highly localized non-hex elements when necessitated by the input feature curve networks (Figure 17). As an additional benefit, the user can be optionally involved in the meshing process, customizing the decomposition via a simple user interaction (Figure 18).

Our method is based on two simple observations. We first note that we can obtain a decomposition that produces well-shaped hexahedral elements by forming a set of *cutting surfaces* bounded by *cutting loops* distributed strategically across the input model's surface. We further note that by selecting a set of cutting loops that are aligned with a surface cross-field and which interpolate the input features, we can produce a decomposition that respects the geometric characteristic of the input model.

Following this observation, our meshing method computes cutting loops and cutting surfaces bounded by them that satisfy the combination of the criteria above. Starting from a cross-field which is aligned to a set of semantic or geometric feature curves (Figure 1a), we extract a set of well-distributed field-aligned loops on the object surface (Figure 1b). We facilitate formation of simple low curvature loops, and corresponding well-shaped cutting surfaces, by balancing field alignment against loop geodesicity. We generate and dynamically replenish a pool of candidate cutting loops. We repeatedly select the most impactful cutting loops from this pool, ones farthest from previously selected ones. We form cutting surfaces that interpolate these loops and adapt to the shape of the input model by using level sets of a smooth volumetric field; we simplify cutting surface geometry by enabling formation of cutting surfaces bounded by multiple loops. We use these surfaces to decompose the volume into coarse simple polyhedral blocks, terminating the process once the blocks satisfy our quality requirements (Figure 1c). We refine the resulting blocks via midpoint subdivision producing a coarse hex-dominant mesh that can then be used to produce high quality hexahedral meshes across a range of resolutions (Figure 1d).

We validate our framework by testing it on multiple inputs of varying complexity, exhibiting a range of geometric and user prescribed features (Section 6). We were able to generate feature-preserving field-aligned meshes across all tested models, and to obtain all-hex meshes on the great majority of them. The minimal element quality of the meshes we produced across all models was 0.33, comfortably above the minimal threshold of 0.2 typically expected by industrial users [Pébay et al. 2007]. We highlight the advantages of our method by comparing our results to those produced using a range of existing strategies.

Our overall contribution is a robust and fully automatic method for block decomposition based hexahedral (or hex-dominant) meshing. We generate comparable or better quality meshes than previous approaches, while guaranteeing feature-preservation and surface-field alignment. This contribution is made possible by our use of field-aware surface loop computation, generation of valid, smooth cutting surfaces that interpolate these loops, and the loop evaluation procedure that leads to robust detection of most effective loops to embed into the block structure.

2 BACKGROUND AND RELATED WORKS

Hexahedral meshing. The generation of high-quality hexahedral meshes is a well researched open problem, which is regarded as extremely difficult among practitioners [Blacker 2000; Owen 2009; Shepherd and Johnson 2008]. Quality meshes are expected to satisfy two core requirements: mesh elements have to be maximally close to cuboids, and the outer surface of the mesh has to closely approximate the input model. Additional requirements include [Blacker 2000]: *geometric matching*, which requires meshes to include all input surface feature curves in the mesh edge network; *boundary sensitivity*, which implies strong preference for meshes aligned with surface curvature directions; and *orientation insensitivity*, which requires the mesh to be independent of the model orientation. Unfortunately, none of the existing methods can robustly satisfy the union of the five requirements above on general inputs.

Traditional approaches to hexahedral meshing can be roughly characterized into a few categories [Blacker 2000; Shepherd and Johnson 2008]: primitive-based, indirect, advancing-front, grid-based, skeleton-based, and decomposition. Primitive based methods and indirect methods are only capable of producing acceptable quality meshes on narrow sets of geometries [Shepherd and Johnson 2008].

Advancing front methods [Kremer et al. 2014; Staten et al. 2005; Tautges et al. 1996] seek to propagate an existing quad surface mesh inward. Recent research on field-based hexahedral meshing can be seen as an extension of this approach: the methods first propagate a tensor field from the surface into the interior of the model and then use this volumetric field to compute a mesh [Jiang et al. 2014; Kowalski et al. 2016; Li et al. 2012; Liu et al. 2018; Nieser et al. 2011; Solomon et al. 2017]. A core advantage of both recent and traditional advancing front approaches is the ability to support all three of the additional requirements above. Unfortunately, both types of approaches do not robustly generalize to models with complex topology. As noted by Liu et al. [2018] existing volumetric field methods require manual intervention to obtain desirable results, even for relatively simple shapes (see Figure 13 in their paper). Similar to these field-based methods, we use a surface cross-field as a starting point, but instead of propagating it into the model's interior, we use it to guide the formation of cutting loops and surfaces, sidestepping the challenge of processing interior singularities, and achieving all the three goals above.

Grid [Lin et al. 2015; Schneiders 1996] and octree-based methods [Ito et al. 2009; Maréchal 2009] use a regular or adaptive grid to mesh the interior of the input models, and use different strategies to connect this mesh to the model's surface. While these methods can robustly handle the core hex-meshing requirements, the meshes

they produce are orientation dependent and are not aligned with curvature directions. Capturing surface features using these approaches requires excessive local refinement (Figure 2 middle), and can result in feature loss.

Polycube-based meshing methods map generic 3D shapes to orthogonal polyhedra (or *polycubes* [Tarini et al. 2004]), mesh this polycube using a regular grid, and then map the resulting mesh back to the original shape [Fang et al. 2016; Fu et al. 2016; Gregson et al. 2011; Huang et al. 2014; Livesu et al. 2013]. These methods produce grid-connectivity meshes in the interior of the model and can be seen as a generalization of the grid-based approach. Similar to grid-based approaches, these methods are orientation dependent and may not match surface features, even after mesh refinement (Figure 2 left).

Automated decomposition techniques seek to cut the object into parts, which can then be meshed conformingly using existing algorithms. Inside-out skeleton [Livesu et al. 2017, 2016] and medial-axis based decomposition approaches [Li et al. 1995; Quadros 2014; Sheffer et al. 1999] fail to generalize to complex shapes. Methods that start from a dense hexmesh and derive a coarse block decomposition from it [Cherchi et al. 2016; Gao et al. 2015, 2017b] may fail to align with features that were not present in the input mesh. Surface-driven block-decomposition techniques use surface features to guide cutting surfaces. Cuts can be used to define both the primal [Blacker 1996; Liu and Gadh 1997; Miyoshi and Blacker 2000; Ruiz-Gironés et al. 2011] or the dual structure [Gao et al. 2018]. Dual methods hardly support feature alignment, because cuts do not directly produce mesh edges, and geometric snapping should be used in post processing to conform with the input features. Primal methods are orientation independent, and frequently satisfy both geometry matching and boundary sensitivity. Unfortunately, both the established [Shepherd and Johnson 2008] and more recent [Kowalski et al. 2012; Wang et al. 2017] automatic block-decomposition methods are limited in the set of geometries they can be applied to. They thus are highly reliant on the sharp feature networks on the model surfaces, and cannot process free-form natural shapes, or shapes with smooth and rounded features. Our method follows the block-decomposition approach popularized by these techniques, and inherits their core advantages. However, contrary to those methods, it does not rely just on the feature curve networks on the input models, and can robustly handle generic free-form models with both smooth and sharp features (Figure 3).

In particular, the torus and the wave in the inset are examples which [Gao et al. 2018] and [Wang et al. 2017], respectively, list as failure cases.

Hex-dominant meshes. A range of methods [Gao et al. 2017a; Lévy and Liu 2010; Ray et al. 2017; Sokolov et al. 2016] support computation of mixed element meshes aiming to minimizing the percentage of non-hex elements while satisfying mesh quality requirements. While recent hex-dominant methods are very robust in terms of the inputs they handle, they still produce a significant percentage of non cuboidal elements [Gao et al. 2017a; Ray et al. 2017]. Our

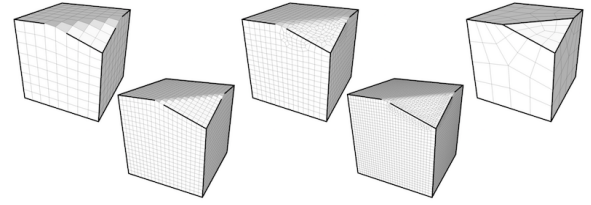


Fig. 2. Polycube-based methods (left), and grid-based methods (middle), fail to conform to features that do not align to the major axes, deviating from the surface and introducing elements with non planar facets. While geometric fidelity can be achieved via refinement, features cannot be matched (bottom). Our method aligns to features in any orientation already at a coarse scale, adjusting the singularity structure of the mesh accordingly (right).

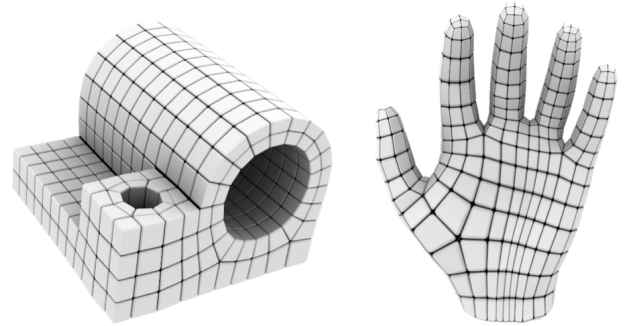


Fig. 3. State of the art tools based on volumetric fields [Liu et al. 2018] require manual intervention to mesh even simple objects like the joint and hand models. Loopy Cuts automatically produces hexahedral meshes with comparable singular structure, without requiring a volumetric field.

approach produces non-hex elements only incident to singular (non valence-3) surface feature vertices (Section 6).

Cross-fields and field-coherent loops. Generating and tracing direction fields on surfaces, or other spatial domains, is becoming a fundamental preprocessing step in numerous applications in computer graphics and geometry processing [de Goes et al. 2016; Vaxman et al. 2016]. Paths traced using most existing methods are not designed to be closed, and are typically terminated when approaching a singularity or another similarly directed path. A range of recent methods seek to connect cross-field singularities with short, field aligned paths [Boier-Martin et al. 2004; Carr et al. 2006; Daniels II et al. 2009]. We trace closed field-coherent loops away from singularities following the approaches of [Campen et al. 2012; Pietroni et al. 2016], which both rely on the formalism introduced in [Kälberer et al. 2007]. We use the discrete graph based structure of [Pietroni et al. 2016] to efficiently trace such loops and compute field-aware geodesic distances.

3 OVERVIEW

The input to our method is a 3D model described by a closed triangle mesh \mathcal{M} , together with a set of line features demarcated as chains of edges in \mathcal{M} . We compute a cross-field on the surface \mathcal{M} using state-of-the-art methodology [Bommes et al. 2009; Diamanti et al. 2014].

We constrain the field to follow the line features in the input and the main curvature directions elsewhere. We incrementally decompose the model into blocks using a sequence of cuts, each of which cuts through the entire model, producing conforming blocks with shared surfaces. Our choice of cutting surfaces is guaranteed to produce blocks whose boundary edges incorporate the input feature curves and are aligned with the input cross-field. The assembly of such blocks, namely their combinatorial structure, will be referred to as a *meta-mesh* \mathcal{MM} ; this structure is updated after each cut and it is formed by cells that correspond to the individual blocks.

Once our incremental cutting results in blocks that are simple enough, we can consider an actual geometrical representation of the meta-mesh \mathcal{MM} composed from polyhedral cells whose faces correspond to portions of the original surface \mathcal{M} or of the cutting surfaces and whose edges and vertices correspond to the intersections between these different surfaces (note that cell faces need not be planar).

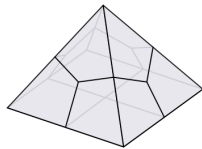
3.1 Decomposition Goals

To obtain the desired output hex (or hex-dominant) mesh quality we aim for the meta-mesh to satisfy the following topological and geometrical criteria. We strictly enforce the Boolean criteria when possible and optimize the continuous ones.

- t1.** Each cell must have genus zero.
- t2.** Each cell face must be bounded by at least three edges.
- t3.** Each vertex of each cell should have valence three.
- g1.** Each cell should be convex.
- g2.** Each cell should be well shaped, i.e. have planar faces and orthogonal edges.
- g3.** Each cell should approximate its corresponding block within a given accuracy.

Criteria **t1** and **t2** guarantee that subdividing each cell would produce a polyhedral mesh. Criterion **t3** guarantees that each cell can be split into hexahedra with a single step of midpoint subdivision. However strictly satisfying it while still incorporating all surface line features may in practice be impossible – see, for instance, the Schneider’s four sided pyramid [Shepherd and Johnson 2008] (inset) – when the combination of sharp and user drawn feature curves results in an input for which no practical hex-mesh exists. We therefore require our method to produce cell vertices of valence three away from irregular feature-curve network vertices, but place no constraints on the valence of cell vertices placed at irregular network vertices. Consequently, absent such vertices our method is guaranteed to produce an all-hex mesh. If such vertices are present the non-hexahedral elements are constrained to the cells containing them.

Criteria **g1** and **g2** control the quality of the meta-mesh cells and indirectly determine the shape of the elements in the final hex mesh. As noted by Owen [2009] a single non-convex element in a hexahedral mesh makes a simulation using this mesh suspect. Finally, criterion **g3** ensures that the meshes produced by refining the meta mesh and projecting the new vertices to the corresponding block surfaces produces meshes with comparable quality to that



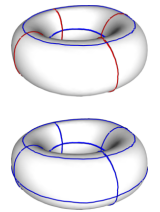
of the cells. We address such criteria indirectly, as explained in the following subsection.

3.2 Algorithm

Informally speaking, we incrementally slice the model by applying cuts, which are defined by loops that strictly adhere to the input line features and follow the input cross field. We update the meta-mesh during this incremental process, and stop the process once the decomposition satisfies the above goals. Once this decomposition is complete we refine it using mid-point subdivision, converting all cells with valence-three vertices into hexahedra. We then refine the mesh to the user designed density and optimize the mesh quality, using off-the shelf optimization code [Livesu et al. 2015].

Generating ordered loops, Section 4. In order to obtain an even, field-aware, distribution of the cuts that respect the input line features, we strategically specify the order in which we choose the cut-defining, or cutting, loops. For this purpose we assemble a preliminary ordered queue of loops that we later scan to generate the cuts that define our decomposition.

We determine the order as follows: first, we insert the loops that are needed to interpolate the input features (Sec. 4.1); we then add loops that, respecting the cross-field, progressively cover the surface in a uniform way (Sec. 4.2). We achieve this increasingly denser and denser uniform distribution by defining a distance over the space of loops, and applying a biased furthest-first sampling procedure using this metric. We bias this sampling procedure to satisfy criterion **t2** by making sure that each loop in the queue is intersected by other loops at three or more points (see inset: the red loops have only two intersections; adding one more loop takes them all to three intersections, giving a configuration sufficient to produce a valid meta-mesh). Thanks to the alignment with the cross field, the selected loops intersect (near)-orthogonally, satisfying criterion **g2**.



Processing the loop queue, Section 5. We build our collection of cutting surfaces by repeatedly extracting the top loop from the ordered queue and using it as a starting point for construction of the cutting surface.

We note that in many instances, such as when forming genus zero blocks starting from a higher genus surface, or when processing models with deep concavities, it may be necessary or simply better to form cutting surfaces bounded by more than one loop (see Figure 7). We therefore develop a loop grouping technique that, given a loop extracted from the queue, finds additional loops such that the combined set jointly bounds a well formed cutting surface. The resulting set of one or more loops partitions the input surface into two disjoint charts. We compute a harmonic field in the interior of the model whose isosurfaces smoothly interpolate these charts. We use the isosurface approximately equidistant from these two charts as our cutting surface (Sec. 5.2).

Once a surface is computed, we use the intersections between it and the current set of blocks to refine the block structure and the meta-mesh by defining new cells, faces, edges and vertices. To

satisfy criterion **t3**, the cutting process constrains new meta-mesh vertices to lie at the intersections of three surfaces, ensuring they have valence three in all their incident cells. Thus all cells away from singular feature-network vertices in our meta-mesh are split into hexahedra during subdivision. Moreover, since surfaces intersect nearly orthogonally, we are able to warrant that criterion **g1** will be satisfied.

We continue to cut the model using new loops from the queue until all cells satisfy our topological requirements and provide a good approximation of the outer shape (criterion **g3**). The quality of approximation is evaluated simply by measuring the difference of area between each external face of the meta-mesh \mathcal{MM} and its corresponding patch of surface on mesh \mathcal{M} .

4 COMPUTING CUTTING LOOPS

Given a cross field \mathbf{X} over a surface \mathcal{M} , we trace field-coherent geodesic paths w.r.t. \mathbf{X} , as in [Pietroni et al. 2016]. A formal definition of field-coherent paths and loops rests upon the stratification \mathcal{M}_4 of \mathcal{M} as defined in [Kälberer et al. 2007] and briefly summarized in Appendix A.1. Informally we define a *field-coherent geodesic loop* through a point $p \in \mathcal{M}$ to be a closed curve that goes through p , is loosely following one of the directions of \mathbf{X} and is as short as possible according to the anisotropic distance defined in Equation 3 (Appendix A.1). Roughly speaking, field-coherency forces a loop to approximately follow the underlying direction field until it gets back to its origin. Requiring a curve to follow \mathbf{X} exactly is unlikely to produce closed loops, as tracing the field directions exactly would usually result in a spiral effect; allowing the curve to drift from \mathbf{X} while remaining as short as possible allows us to use \mathbf{X} as a guide to extract consistent loops.

Each point p on \mathcal{M} which is away from a field singularity can be crossed by exactly two field-coherent geodesic loops, which are orthogonal to one another at p (disregarding the traced curve's orientation). We consider the set \mathbf{L} representing the space of all loops for any point $p \in \mathcal{M}$.

We incrementally build a queue of loops $\mathcal{L} \subset \mathbf{L}$, which will be scanned to generate the cuts, as follows:

- (1) We initialize \mathcal{L} with loops that incorporate a subset of the input curve features (Sec. 4.1);
- (2) We extend \mathcal{L} using a sampling process that aims to select loops that intersect orthogonally and are evenly distributed on \mathcal{M} . This step is based on furthest sampling on \mathbf{L} and requires the definition of a suitable distance on the space of loops (Sec. 4.2).

Since the space of loops \mathbf{L} is infinite, the sampling process is discretized by forming an extensive *pool of loops* \mathcal{P} from which we sample, and which is built dynamically during the selection process (Section 4.3).

4.1 Generating Loops Incorporating Line Features

The extraction and classification of sharp input features is out of the scope of this paper and they are considered part of the input. Our initial feature set consists of both open and closed curves. We form a feature curve network by placing vertices at feature curve intersections, sharp corners, and dangling end-vertices of open

curves. We break the curves into segments bounded by vertices and treat each segment as a separate curve in the process below. We classify each feature curve as *concave*, *convex* or *flat* based on the average dihedral angle along it. We employ this classification to determine the number of cutting loops we want to incorporate each feature curve into: we expect each flat feature to belong to a single cutting loop and expect each concave feature to belong to two cutting loops. We do not perform cuts along the convex features, but use them to initialize the meta-mesh (Section 4.4). This cutting loop formation strategy fosters the formation of as-right-as possible dihedral angles for all blocks incident to a given feature (Figure 9).

We initialize the cutting loop queue \mathcal{L} as follows:

- (1) We add to \mathcal{L} all loops formed by closed non-convex features.
- (2) We extend each open concave feature into two complete loops by loop tracing and extend each open flat feature into one loop (Appendix A.1).
- (3) For each convex feature that has one dangling endpoint we try to extend it into a loop or, if not possible, we trace a loop through that endpoint in the direction orthogonal to the feature curve, adding it to the queue. This step helps eliminate vertices of valence 1 or 2 on the subsequent meta-mesh which would induce non-hexahedral blocks.

Figure 4 shows some examples of concave line features and their extension to form loops. Note that loops should not pass through singularities (see Appendix A.1), while the endpoints of an open feature f are likely to lie at singularities. We get around this issue by tracing two loops ℓ_1 and ℓ_2 that run parallel to the feature f along its two sides, and infinitesimally close to it. The portions of the loops ℓ_1 and ℓ_2 corresponding to the feature f are constrained to follow it. After completion these portions are snapped to f , while the remaining portions are left free to follow the field elsewhere. Since the endpoints of f might be singularities, the loops ℓ_1 and ℓ_2 may take different routes (see Figure 4.c-d). We favor the formation of loops that encompass more than one line feature (see Figure 4.e), by introducing a bias during loop tracing, which reduces the length of curves running along curve features (see Section 4.3 and Appendix A.2 for details).

We discard self intersecting loops. When tracing loops we prevent any new loop from tangentially intersecting, or partially overlapping with, another loop or feature curve (other than the one it lies on). See Appendix A.1 for a formal definition of tangential and orthogonal intersections. To this end we form a set of constrained edges \mathcal{CF} initialized with all convex feature curves. For any newly formed loop we prevent it from tangentially intersecting curves in \mathcal{CF} or \mathcal{L} .

4.2 Sampling Loops

We augment the queue \mathcal{L} with additional loops in order to obtain a fairly regular distributions of loops over \mathcal{M} and to allow for formation of blocks that satisfy the topological constraints in Section 3.1. We define an *arc* as a portion of a loop $\ell \in \mathcal{L}$ that lies between two consecutive intersections of ℓ with other loops of \mathcal{L} . To satisfy criterion **t2** we require each loop to consist of at least three arcs.

4.2.1 Loop Space Distance. In order to evenly sample loops from the space \mathbf{L} , we introduce a notion of (non-symmetric) distance

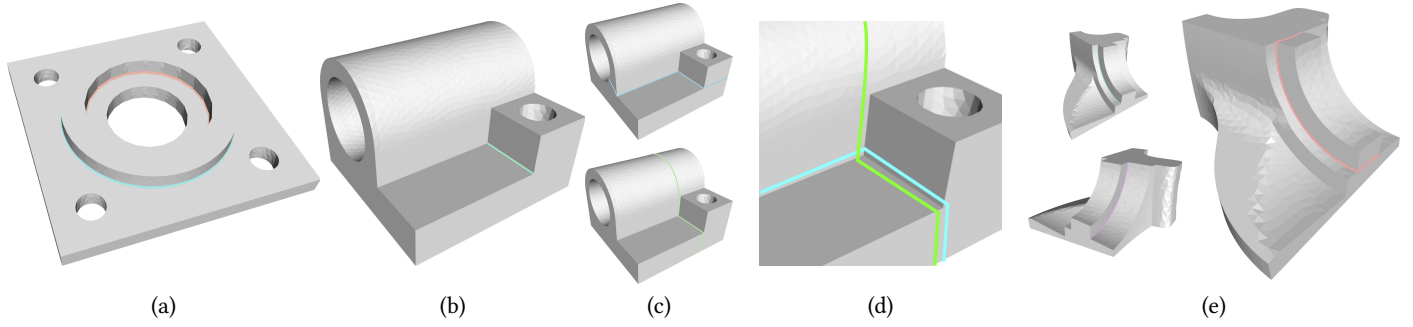


Fig. 4. (a) Closed concave curve features; (b) an open curve feature; (c) the open curve feature is extended to form loops; (d) a closeup on field topology of traced loops (displaced from the feature in the rendering); (e) a concave loop connecting multiple concave incomplete sharp features (left, the open features; right, the loop connecting them).

between loops, as the average over one loop of the shortest distance from each of its points to the other loop. Let ℓ_i and ℓ_j be two loops, then we define:

$$d(\ell_i, \ell_j) = \frac{1}{|\ell_j|} \int_{\ell_j} \text{dist}(\ell_i, p_\theta) dp_\theta \quad (1)$$

where $\text{dist}(\ell_i, p_\theta)$ is the length of the shortest field-coherent geodesic path joining a point of ℓ_i to p_θ . In order to get an intuition for this distance, consider that two roughly parallel loops on \mathcal{M} are close to one another, while loops that are either intersecting orthogonally, or wind about different handles of an object (of non-null genus) are usually far apart.

Now considering a set of loops $\mathcal{L} = \{\ell_1, \dots, \ell_k\}$, and a loop ℓ not belonging to \mathcal{L} , we can generalize

$$d(\mathcal{L}, \ell) = \frac{1}{|\ell_j|} \int_{\ell_j} \min_{\ell_i \in \mathcal{L}} \text{dist}(\ell_i, p_\theta) dp_\theta, \quad (2)$$

hence the notion of farthest loop $\bar{\ell}$ from \mathcal{L} is well-defined as

$$\bar{\ell} = \text{argmax}_{\ell \in \mathcal{L}} d(\mathcal{L}, \ell).$$

4.2.2 Loop Insertion. We extend the queue \mathcal{L} incrementally through a process of farthest point sampling. We form a discretization \mathcal{P} of the infinite space of loops \mathbf{L} , which we refer to as the *pool*, which is built dynamically and used to sample loops to build \mathcal{L} as follows. We define the set $\bar{\mathcal{L}} = \mathcal{L} \cup C\mathcal{F}$ as the set that contains all loops in \mathcal{L} together with the set of all convex curve features. We form the initial pool as follows.

- (1) We sample all curves of $\bar{\mathcal{L}}$ at fixed intervals and, for each sample, we trace orthogonal loops that we add to \mathcal{P} . Traced loops are constrained to avoid tangential intersections with the elements of $\bar{\mathcal{L}}$;
- (2) We perform a Poisson point sampling on \mathcal{M} [Corsini et al. 2012] to obtain a set of seeds \mathbf{P} and, for each seed p , we trace the two orthogonal loops, each constrained by the elements of $\bar{\mathcal{L}}$ as above, and we add such loops to \mathcal{P} .

Each time we add a new loop ℓ to \mathcal{L} , we replenish the pool with new loops obtained by sampling ℓ as described in item (1). When adding loops to \mathcal{P} , we prevent them from tangentially intersecting any loop in \mathcal{L} .

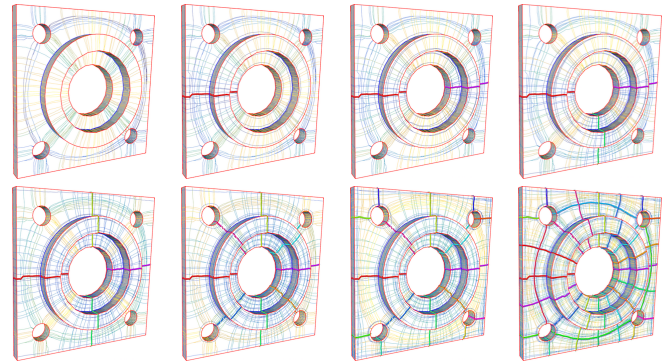


Fig. 5. The queue of loops \mathcal{L} is created iteratively (red lines). The thin lines denote loops in the pool \mathcal{P} , where color denote distance from the features already present in \mathcal{L} : blue close, yellow far.

We add loops from the pool to the queue \mathcal{L} using the following priority rule. Let $\hat{\mathcal{L}}$ be the subset of \mathcal{L} made of loops that are formed by less than 3 arcs. We give higher priority to those loops in \mathcal{P} that intersect at least one loop in $\hat{\mathcal{L}}$; among them, we select the loop ℓ that maximizes its distance from all loops in $\bar{\mathcal{L}}$ and we add ℓ to \mathcal{L} . Next, we remove from \mathcal{P} all loops that intersect ℓ tangentially, and retrace them from their sources in \mathbf{P} , constrained to the updated $\bar{\mathcal{L}}$.

This step can be repeated at will and fosters the formation of a queue \mathcal{L} that contains loops with at least three arcs and are uniformly distributed over \mathcal{M} . Figure 5 shows a few steps of loop generation (see Section 4.3 for details). Note in Figure 5 how both the collection of loops in \mathcal{L} and the pool \mathcal{P} become progressively more dense as the process goes on. The generation of loops is stopped as criteria **t2** and **g3** are both satisfied (where geometric fidelity **g3** is tested on the patches intercepted by the network of loops on mesh \mathcal{M}); in order to speedup the process, criterion **g3** is not tested until **t2** is satisfied at all loops.

4.3 Discrete Loop Tracing

To efficiently and robustly implement the tracing procedure and furthest sampling process described in the two previous sections, we

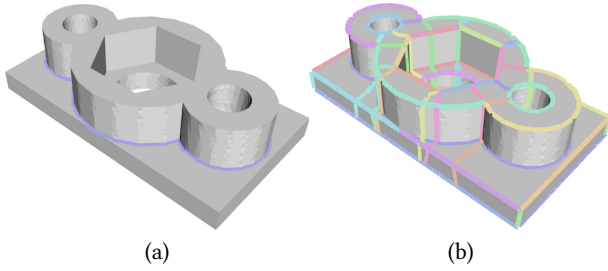


Fig. 6. (a) a loop spanning across multiple concave features; (b) a mesh where all sharp features have been sampled.

trace field-coherent geodesic loops with the discrete graph-based approach of [Pietroni et al. 2016], which brings to the stratified structure \mathcal{M}_4 (Appendix A.1) the technique of [Lanthier et al. 2001] to evaluate geodesic paths and distances. In short, in [Lanthier et al. 2001] shortest paths and distances are found by a Dijkstra search on an extended graph \mathcal{G} , which is built over \mathcal{M} edges and vertices, plus Steiner points sampled on edges and arcs connecting vertices of \mathcal{M} and Steiner points across each triangle. In our case, four point-arrows are generated per vertex and per Steiner point, which are properly arranged on \mathcal{M}_4 , and just field-coherent arcs connecting them are considered. The graph \mathcal{G} is built once, and used in all subsequent processing. One important advantage of this method is that crossings and overlaps of paths can be handled in a robust, combinatorial way that does not involve numerics: it is possible to precisely identify whether two paths intersect orthogonally or tangentially by simply comparing arcs that belong to the same triangle of \mathcal{M} and checking their underlying direction fields. Thus during tracing we prevent any new loops from tangentially intersecting loops in \mathcal{L} by blocking Dijkstra propagation along arcs in \mathcal{G} that are orthogonal to those arcs belonging to paths already in \mathcal{L} .

Loop Space Distance. Given a queue of loops \mathcal{L} , we set a source for each node of graph \mathcal{G} traversed by each loop $\ell_i \in \mathcal{L}$ and we run a Dijkstra propagation. The distance $d(\mathcal{L}, \ell)$ from any other loop ℓ is computed easily by collecting distances at all nodes traversed by ℓ after propagation. Note that a single Dijkstra propagation is sufficient to set distances at all nodes of \mathcal{G} , thus it is sufficient to evaluate distances from all loops.

Extending curve features to loops. At the beginning of the process, all open line features must be extended to loops, as described in Section 4.1. Since most such features join singularities of \mathbf{X} , we cannot directly extend them from their endpoints, which are not represented in graph \mathcal{G} . Therefore, we proceed by tracing loops that run parallel to each feature, and we snap such loops to the features later on. This procedure is described in more details in Appendix A.2.

A complete set of sampled sharp features for a mesh is shown in figure 6.b. A sequence showing the first three loops sampled for a simple cube is shown in figure 5.

4.4 Convex Features and Meta-Mesh Initialization

We initialize the meta-mesh \mathcal{MM} as being formed of a unique cell, with surface \mathcal{M} , embedding on it all convex features as edges, and their corners and endpoints as vertices; faces of \mathcal{MM} are the components of \mathcal{M} that are disconnected by this network of convex features (possibly, there can be a single face with cuts). For each convex feature that has one dangling endpoint we extend the feature along its direction to form a loop. We add the edges along this loop to the meta-mesh, updating the face structure accordingly.

5 MODEL CUTTING

Our cutting method receives as input the current top loop ℓ_i in the loop priority queue, and uses it to form a cutting surface that partitions the current model \mathcal{M} into two disjoint parts, refining the intersected blocks and their corresponding meta-mesh cells. Each cutting surface is bounded by a set of loops that includes ℓ_i . The cutting process involves three major steps: loop grouping, cutting surface computation, and block set and meta-mesh refinement.

5.1 Loop grouping

While a cut bounded by a single loop is enough to halve a genus zero object, additional loops may be necessary to cut in half higher genus shapes. Moreover, using a single loop may produce highly non-planar cuts in the presence of deep cavities. Using surfaces with multiple boundary loops in such cases allows for cuts with less geometric distortion (Figure 7). We address both scenarios by forming cutting surfaces with multiple boundary loops, producing better shaped blocks. We group loops together using a combination of topological and geometric criteria.

We observe that, from a cutting perspective, we need to distinguish between three different types of loops, which can be roughly classified according to the interaction between the outward loop curve normals and their coincident surface normals (Figure 8):

- **Type I** loops conceptually lie outside the object, and have outward normals well aligned with the surface normal. These loops may bound a well shaped, or near planar, cutting surface on their own, and form the majority of our cutting surface boundaries.
- **Type II** loops have normals that point in the opposite direction to the surface normals, and are typically located inside tunnels or cavities. To obtain a well shaped cutting surface, these loops always require a cutting mate of type I, which defines the outer boundary of the same cutting surface, and may occasionally be grouped with other loops of same type, generating a surface with multiple holes.
- **Type III** loops have normals that lie close to the surface tangent plane. To provide a non-degenerate partition of the object, they need to be paired with a cutting mate of the same type, to jointly form an approximately cylindrical cutting surface.

Note that this characterization is not formal, but rather a tool to predict the shape of the surfaces that would result from using each loop or a set of loops as a boundary of a cutting surface. In fact, a cut that interpolates two loops of type III and a cut that interpolates one loop of type I and one loop of type II are topologically equivalent

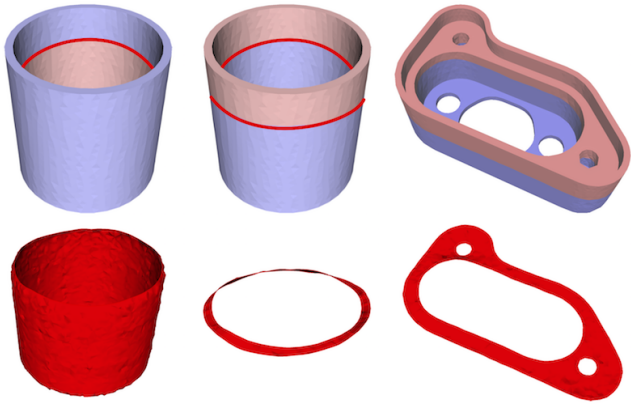


Fig. 7. Left: halving a genus zero object using a loop located inside a cavity generates a highly non-planar cutting surface (red). Middle: matching the inner loop (type II) with its best matching loop outside the same cavity (type I) produces a better cut. Right: pairing one external loop with multiple inner loops we provide high quality surface cuts for complex shapes containing a variety of tunnels and cavities.

(they are both generalized cylinders with two disjoint boundaries); but while in the former case the cylinder has a well defined inner axis, in the latter case it may be completely foreshortened with two coplanar boundaries.

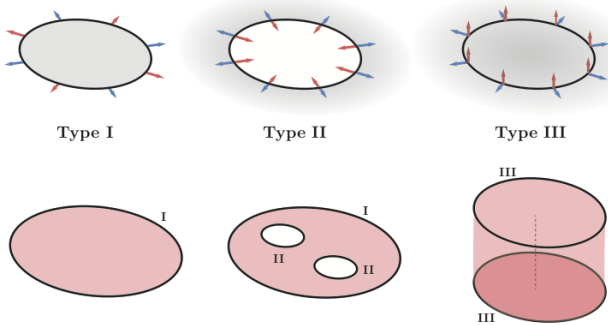


Fig. 8. Top: loops are grouped according to the type of cut they induce on the object, which can be inferred by studying the relation between the outgoing loop normals (blue) and the surface normals (red). Bottom: loops whose normals are roughly orthogonal to the surrounding surface (type I and II) can be combined together to split high genus objects. In particular, type II loops arise in tunnels and deep cavities, and always require a pairing loop of type I for cutting. Loops whose normals lie in the surface’s tangent plane (type III) require a complementary loop for cutting and can be matched only with loops of the same type.

Loop assessment. To assign a unique type to each loop we study the relation between its normals and the surface normals (Figure 8). We compute loop normals using the curve’s Frenet frame, oriented according to the winding order that provides normals that largely point away from the loop’s center of mass. We integrate the dot product between loop and surface normals, and perform the classification

by applying a symmetric threshold centered at 0 to discriminate between the three types. Values higher than 0.3 denote type I loops; values lower than -0.3 denote type II loops; and values in between denote type III loops.

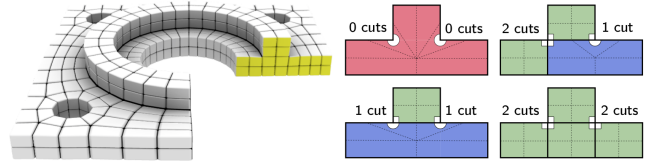


Fig. 9. Concave features have an internal angle larger than π , and always require two orthogonal cutting surfaces to produce a high quality block decomposition. Note that the two cuts at each concavity interpolate two loops of different types: the horizontal cut interpolates two loops of type I and II; the vertical cuts interpolate two loops of type III each. Thin dashed lines show how the decomposition would look like after one step of midpoint subdivision.

Note that if a loop spans a sharp geometric feature there will be a mismatch between the surface normals on one side of the loop and the normals on the opposite side. As explained in Appendix A.2, our loop tracing method always produces two loops along each concave feature on its opposite side. Each loop is infinitesimally close to the feature, and is parallel to it without ever crossing it. Consequently each such loop has a different surface normal and induces different cuts. At the same time, in geometric space the portions of the loops along the feature completely overlap. Thus along closed features such as the two concave rings of the Bearing Plate, the loops generate two cuts orthogonal to one another emanating from the same geometric loop (Figure 9).

Grouping. Starting from a loop ℓ_i , we wish to find the smallest set of complementary cutting loops that jointly with this loop cut the surface in half and produce a cutting surface whose shape is most reflective of the loop’s type. If the loop ℓ_i is of type I or II, we seek to obtain a cutting surface that is as planar as possible, whereas if the loop ℓ_i is of type III we wish to obtain a cylinder-like cut. We reflect this preference using a loop pairing metric defined as follows:

$$E(\ell_i, \ell_j) = \begin{cases} E_{\text{plane}}(\ell_i, \ell_j) & \text{if } \ell_i, \ell_j \text{ have both type I or II} \\ E_{\text{cyl}}(\ell_i, \ell_j) & \text{if } \ell_i, \ell_j \text{ have both type III} \\ \infty & \text{otherwise} \end{cases}$$

where the terms E_{plane} and E_{cyl} measure the similarity between the loops spanning planes or cylinders, respectively. Specifically, E_{plane} is ϵ if ℓ_i and ℓ_j span the same approximating plane, and grows proportionally to the angular and euclidean distance between the planes they span. E_{cyl} is ϵ if ℓ_i and ℓ_j span the same approximating cylinder, and grows proportionally to the angular distance between their axes and the ratio between their cylinder radii. Both metrics are defined in the range $(0, 1]$ and implemented using Gaussian functions. The details on the computation of the approximating planes and cylinders and the metric used to assess their similarity are provided in Appendix B.1.

Given an initial loop ℓ_i , we determine the optimal set of cutting loops by computing a binary labeling of the surface \mathcal{M} that

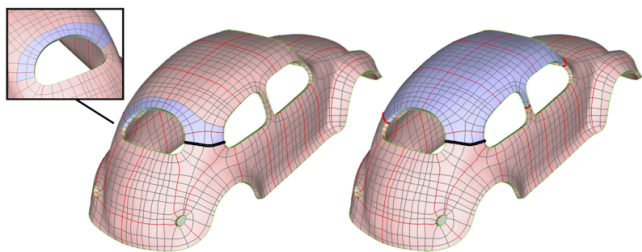


Fig. 10. Left: Using a loop that does not have a good geometric matching with any other loop in the queue may produce globally inconsistent bi-partitions, where only a portion of the edges participating in a loop are selected for cutting (closeup, bottom left corner). Right: when the geometric grouping fails, we use topological grouping as a backup strategy. This strategy minimizes cut length and therefore performs minimal cuts around topological handles (right).

minimizes

$$E(\ell_i) = \sum_{\ell_j \in \mathcal{L}} E(\ell_i, \ell_j),$$

and is constrained to have different labels along the opposite sides of ℓ_i to guarantee that the boundaries of the bi-partition include it. We compute the solution using a min-cut formulation applied to the dual of mesh \mathcal{M} . Cuts along mesh edges (arcs in the dual graph) that do not belong to any loop receive ∞ costs, whereas a cut along a mesh edge e that belongs to some loop ℓ_{j_e} contributes to the energy proportionally to the ratio between its length and the total length of the loop it belongs to

$$E_e(\ell_i, \ell_{j_e}) = E(\ell_i, \ell_{j_e}) \cdot \frac{|e|}{|\ell_{j_e}|}$$

The minimizer of $E(\ell_i)$ automatically provides the smallest set of additional loops that globally halve \mathcal{M} and are geometrically best aligned with ℓ_i . We compute the solution using the min-cut implementation provided by [Boykov and Kolmogorov 2004; Boykov et al. 2001; Kolmogorov and Zabih 2004]. Note that minimizing E at local (per edge) level may produce inconsistent global results, where only a subset of the edges participating in some loop is selected for cutting (Figure 10). Empirical observations indicate that this happens only if there are no good geometric matches for ℓ_i in the loop queue \mathcal{L} . We recover from these pathological situations by using a backup strategy, which consists in minimizing the total length of the cuts, as detailed in Appendix B.2. The backup strategy is purely topological, and essentially cuts along all topological handles that are necessary to globally halve the shape with as short as possible cuts. Since loops are geodesic, cutting along a whole loop in general produces a shorter boundary than partially cutting along multiple loops, and therefore a valid cut set is usually found. If no valid cutting loop set can be found also with the backup strategy, the initial loop is discarded.

Handling Cavities. The loop grouping as described above introduces complementary loops in the cut set only if ℓ_i does not bi-partition the surface of \mathcal{M} alone. If ℓ_i is a separating loop no complementary loops will be found, as they would increase the energy. As a result, loops of type II located inside cavities will not receive

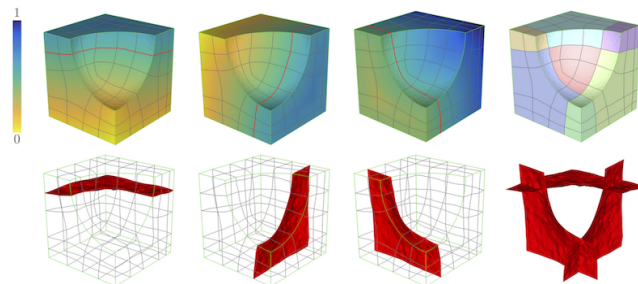


Fig. 11. Three solid cuts computed with our algorithm. Cuts are defined as level sets of a harmonic function that evaluates to 0.5 along the cutting loop, is higher on one side of the cut, and lower on the opposite side. Cuts are embedded into the connectivity of the mesh, producing a labeling that induces a solid decomposition of the object (right).

a matching loop of type I, producing highly non planar cutting surfaces that induce a poor block decomposition (Figure 7, left). Thus we first locate all type II loops in our queue and apply the grouping process from them to other loops. If one of those loops is subsequently pulled from the queue we use its previously computed group as the cutting surface boundary. To provide a quality decomposition of complex objects containing a variety of tunnels and cavities, several inner loops of Type II may need to match to the same outer loop of Type I at once, producing a single surface cut with many holes inside (Figure 7, right). We obtain the desired effect by imposing specific boundary conditions on the min-cut algorithm. For each loop of Type II, we first compute its best geometric match of Type I using E_{plane} . We then cluster together all loops of Type II that match the same Type I outer loop, and each time any of these loops is used for cutting, we force the min-cut step to cut through all of them. Similarly, for each loop of Type III that does not surround a handle (i.e. it is contractible), we find its best geometric matching according to E_{cyl} , and force min-cut to include both such loops in the bi-partition.

5.2 Solid cut

Given the set of cutting loops $C = \{\ell_0, \ell_1, \dots, \ell_n\}$ that bi-partitions the surface of the object, we extend the cut to the interior by defining it as the level set of a volumetric harmonic function that aligns with C . Harmonic functions satisfy the maximum principle, which ensures that if the function is non flat, then maxima and minima arise only at the boundaries of the domain and never in the interior. By prescribing Dirichlet boundary conditions on the surface \mathcal{M} , we can therefore control the topology of the cutting surface, and guarantee that it interpolates all the cutting loops in C , is manifold, and does not interpolate any other points on the model's surface.

Considering the bi-partition of the surface \mathcal{M} induced by the loop set C , we denote V_C as the vertices of these loops, V_l as the vertices to the left of C , and V_r as the vertices to the right of C . We then solve for the volumetric harmonic function $\Delta f = 0$, subject to

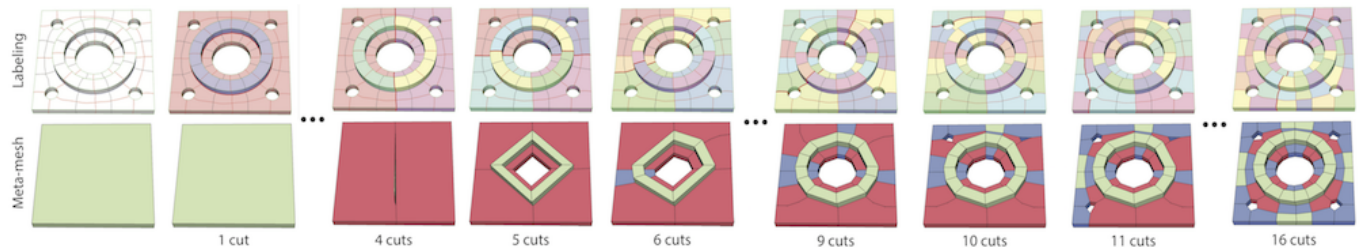


Fig. 12. Progressive generation of the meta mesh for the Bearing Plate. Top: the labeled tetrahedral mesh; bottom: its corresponding meta-mesh (hexa in green, prisms in blue, other cells in red).

the following Dirichlet boundary conditions

$$f = \begin{cases} 0.5 & \text{if } v \in V_C \\ 0.5 + d(v, C)/2D & \text{if } v \in V_l \\ 0.5 - d(v, C)/2D & \text{if } v \in V_r \end{cases}$$

where the 0.5 level set of f defines the cutting surface bounded by our set of loops C (Figure 11); and $d(v, C)$ denotes the distance between each surface vertex v and its closest loop in the cut set C , measured using a Dijkstra search on the graph of edges of the volumetric mesh \mathcal{MV} . The normalization factor D is used to bound the function to the range $[0, 1]$, and is the maximum distance from a surface vertex to the set of loops C . We implement the Δ operator as a simple combinatorial Laplacian, using uniform weights for all vertices in the one ring. The choice of combinatorial Laplacian was dictated by the need for solution robustness. Our cutting surfaces are embedded into the connectivity of the tetrahedral mesh and cut across mesh edges. This embedding process progressively worsens the shape of the tetrahedral mesh elements as more cuts are introduced. While the popular cotangent Laplacian is geometry-aware and produces smoother level sets on well shaped meshes, our experiment show that using it on poor quality meshes results in ill-conditioned and numerically unstable linear systems. In contrast, the combinatorial Laplacian is robust to meshing defects, and always yields a well-conditioned positive semi-definite matrix. While in theory it is not geometry-aware, in practice the cutting surfaces we obtained were always good enough for our purposes, even when the tetrahedral elements were poorly shaped.

5.3 Meta-mesh update

The meta-mesh \mathcal{MM} is initialized as a single volumetric cell, which incorporates on its boundary all the input feature lines as edges, their endpoints as vertices, and the surface patches of \mathcal{M} that are disconnected by them as faces. Solid cuts are progressively embedded into the connectivity of a tetmesh by splitting all the edges traversed by the 0.5 level set (Figure 12). As a result, each cut is a collection of triangular facets of \mathcal{MV} that separates pairs of tetrahedra incident at them at both sides. Using these facets as boundaries and performing exhaustive region growing on the tetmesh we produce and maintain a labeling of tetrahedra defining the volumetric cells of our decomposition. We extract the faces, edges and vertices of the associated meta-mesh from this labeling. Each face of the tetmesh at the interface between two different labels (including the null label conventionally assigned to outer space) is labeled with such

pair of labels, and all tetmesh faces with the same pair of labels are gathered to form a meta-mesh face; then edges of the meta-mesh are obtained by gathering chains of edges of the tetmesh that have the same set of two or more incident faces of the meta-mesh. Finally, tetmesh vertices incident on three or more edges of the meta-mesh are classified as meta-mesh vertices. In case topological inconsistencies arise while intersecting a cutting surface with the current meta-mesh, we fix them as explained in Appendix B.3.

6 RESULTS

We validate our method on a range of models of different complexity, both mechanical and organic, and showcase 31 fully hexahedral meshes and just one hex-dominant mesh throughout this paper. We report numerical statistics in Table 1. Loopy Cuts produces meshes with a complex singularity structure, enabling them to conform to the input features and at the same time provide extremely high per-element quality, often much higher than alternative hexmeshing techniques (e.g. Figure 15). We demonstrate our ability to conform to a variety of features, both geometric (Figure 13) and synthetic (Figure 16). Our pipeline creates pure hexahedral meshes given surface feature networks with all valence three vertices. Our midpoint subdivision introduces non hexahedral elements only on meta-mesh cells that are incident at vertices with a valence different from three (Figure 17). These configurations seldom occur in practice, and in our experiments we produced only one hex-dominant mesh containing four hybrid elements (less than 1% of total elements count). As shown in Figure 14, we generate full hexahedral meshes even when state of the art hex-dominant meshing techniques introduce a significant amount of hybrid elements. In general, these techniques consistently produce meshes with a much lower percentage of regular elements (72% to 91% hexahedra for [Gao et al. 2017a], and 33% to 95% hexahedra for [Sokolov et al. 2016]), and contain complex hybrid elements that may have up to 40 facets (see Table 1 in [Gao et al. 2017a]).

Customization. Loopy Cuts is fully automatic, but can optionally be used in interactive mode to allow the user to customize the block decomposition. In Figure 18 we show a result obtained with manual interaction, where we guided the loop grouping and cut sequence to obtain a perfectly symmetric mesh with high anisotropy along one direction. We provide this control by enabling three interactive operations that can be activated via a trivial point-and-click user interface. The user can:



Fig. 13. Hexahedral meshes produced by Loopy Cuts in automatic mode. Small insets showcase meta-meshes (hexa in green, prisms in blue, other cells in red).

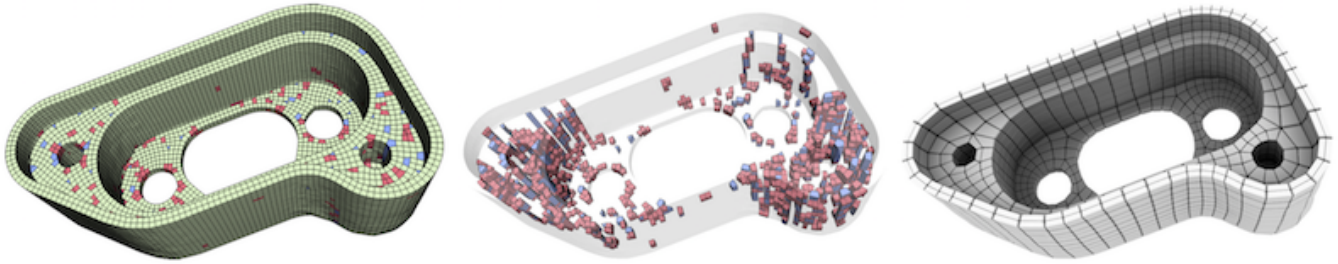


Fig. 14. Left: a hex-dominant mesh produced with [Gao et al. 2017a] (hexahedra in green, prisms in blue, other polyhedra in red). Middle: the mesh contains many non cuboidal elements, both in the interior and along the exterior. Non hexahedral elements can be arbitrarily complex: in this model the most complex element counts 17 faces. Right: our result.

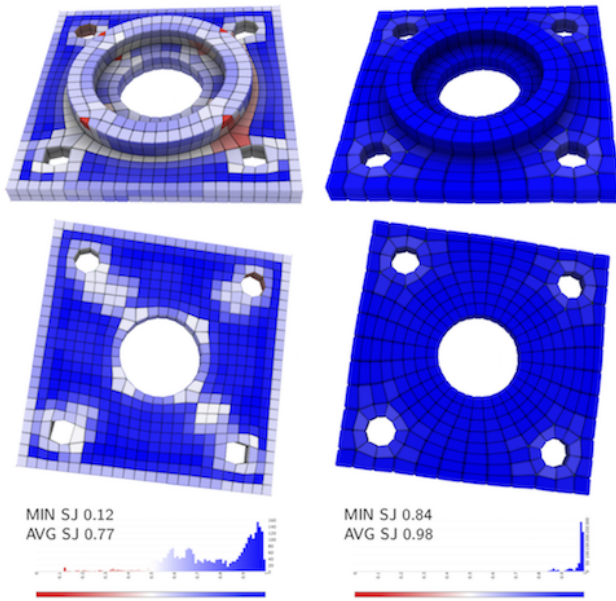


Fig. 15. Comparison between a state-of-the-art PolyCube-based method [Livesu et al. 2013] (left) and Loopy Cuts (right). Even though the PolyCut mesh is almost four times larger than ours (2.7K vs 0.7K elements), it is not as effective at capturing the sharp features on the object (see the square-like little holes at the bottom). Meshes derived from our block-decomposition naturally align with features, and yield a quality mesh with much higher average and minimum scaled Jacobians.

- Prescribe a customized cut sequence. Each time a loop is selected for cutting, the system automatically finds complementary loops, and the volumetric cut is performed;
- Manually pair loops for cutting. Note that this could also be used to accumulate multiple cuts into one (e.g. the cuts that separate the dents from the pinion wheel in Figure 18 were made all together, while the automatic approach would have processed them in sequence);

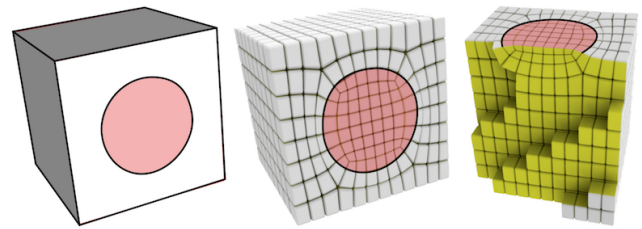


Fig. 16. Left: an input cube with a user-demarcated circular feature on one of its faces. Middle: the hexahedral mesh produced by Loopy Cuts. Right: cut through view showing the inner mesh connectivity (the cube is rotated to highlight the singular structure beneath the circular feature).

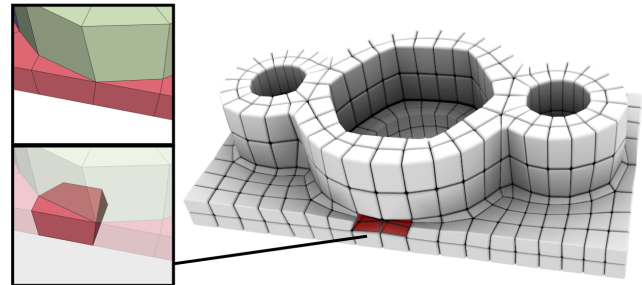


Fig. 17. Left: Loopy Cuts may introduce mixed elements if surface features that are not cut through form non-valence-three vertices with respect to a meta-mesh cell. Right: the resulting mesh after midpoint subdivision (mixed elements are in red).

- Mark a loop as a new *convex feature*. Such a loop will then be incorporated in the meta mesh as a chain of surface edges that split faces, but the meta mesh will not be cut through it.

An additional indirect form of customization can be obtained by editing the guiding surface field with user-interactive tools such as the one proposed in Instant Meshes [Jakob et al. 2015]. Such tools can be used to prescribe additional soft constraints on the meshing process promoting alignment to secondary features or symmetries (Figure 19).

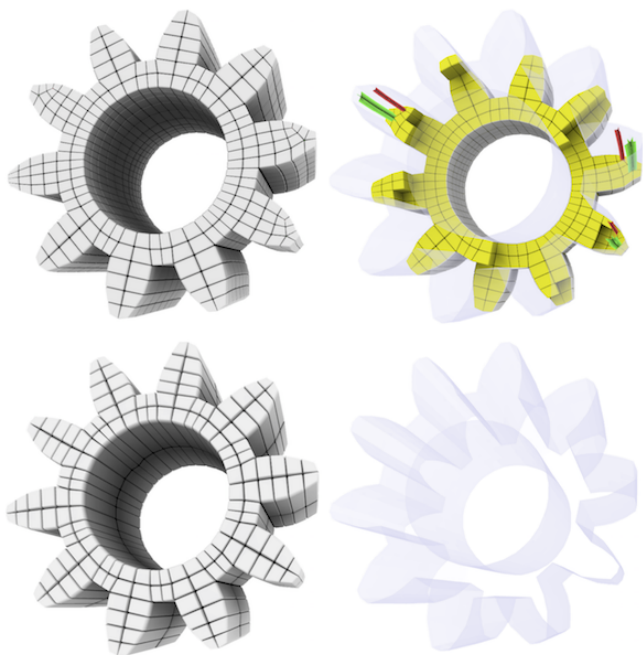


Fig. 18. Top: in fully automatic mode the cut set and loop grouping used by Loopy Cuts produce a result where different dents have different mesh connectivity, and a few singular chains of edges appear in the interior. Bottom: by manually selecting the cut set (from the automatically generated sequence) and performing guided grouping we produce a perfectly symmetric mesh with no singularities; instead high anisotropy is introduced along the height of the wheel (no horizontal cuts were performed, the only visible cut is due to midpoint subdivision).

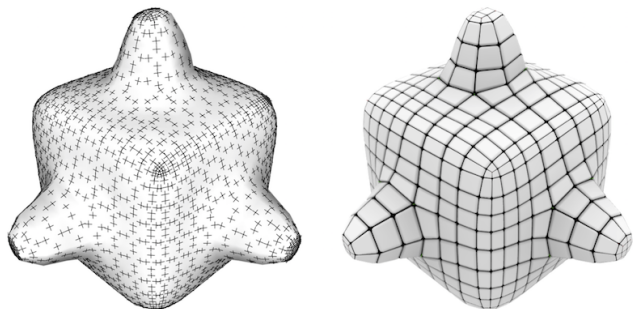


Fig. 19. The volumetric meshes generated by Loopy Cuts are guided by a surface field. Leveraging existing field processing tools we can therefore control the meshing process. Here we encoded in the cross field the symmetries of the object (from [Panozzo et al. 2012]) that were then transferred to the hexahedral mesh.

Implementation details. We implemented *Loopy Cuts* as a single threaded C++ application, using Tetgen [Si 2015] for tetrahedralization, and Eigen [Guennebaud et al. 2010] for numerics. Cross fields aligned to line features and surface curvature were computed using MIQ [Bommes et al. 2009] and the PolyVector Fields method [Diamanti et al. 2014]. Sharp creases were automatically detected by

Model	Δ	Cuts	Meta-mesh			Output mesh	
			H	P	O	H	SJ
3holes	19k	13	64	16	0	1K	.50/.87
anchor	11k	16	44	28	9	0.7K	.33/.85
anti backlash nut*	13k	34	77	14	16	0.7K	.43/.84
bamboo pen	36k	20	76	38	0	0.8K	.72/.93
bearing plate	10k	16	43	12	16	0.7	.84/.98
beetle	70k	34	154	38	0	1.6K	.50/.95
blech	60k	42	132	30	0	1.3K	.64/.96
block	28k	15	33	32	10	0.6K	.41/.82
cap thing	57k	15	68	18	6	0.8K	.56/.92
cube minus sphere	4k	3	17	4	1	0.2K	.62/.97
cube 2 colors	2k	11	56	16	8	0.8K	.50/.96
spiky cube	6k	22	136	72	56	1.8K	.57/.93
delta arm base	37k	22	52	38	12	0.9K	.50/.77
double torus	32k	11	0	88	4	0.6K	.49/.81
fandisk	7k	17	126	11	1	2K	.48/.85
hand	20k	29	31	82	37	1K	.33/.83
hinge	19k	13	56	14	2	0.6K	.52/.94
impeller	24k	31	96	96	0	1.7K	.36/.88
joint	9k	12	56	12	0	0.6K	.77/.97
knob	14k	10	88	12	0	0.7K	.82/.97
lever arm	9k	23	36	32	4	1.2K	.54/.92
lock	42k	22	124	58	18	1.7K	.38/.85
motor tail	15k	45	177	53	0	2K	.51/.95
pinion	43k	40	230	30	0	2K	.41/.95
pinion (manual)	43k	12	40	0	0	0.3K	.66/.95
rod	9k	15	108	46	4	1.2K	.72/.95
sculpture	32k	25	80	8	0	0.7K	.77/.97
shaft	30k	10	20	32	8	0.6K	.44/.92
torus	4k	12	65	52	0	0.8K	.82/.93
toothbrush holder	13k	26	43	38	0	0.7K	.62/.93
trebol	13k	10	0	15	17	0.2K	.47/.77
wave	3k	11	40	16	16	0.5K	.60/.93

Table 1. Statistics of our method. For each dataset we report: the number of faces of the input mesh Δ , the number of cuts being performed; the number of hexa (H), prisms (P) and other elements (O) in the meta mesh; the number of hexa (H) in the final mesh; minimum and average Scaled Jacobian (SJ) of the hexahedral elements of the mesh. (* this model is mixed, and contains 4 non-hexa elements).

thresholding dihedral angles, whereas other features were manually marked. Note that both field computation and feature detection are external to the algorithm; alternative techniques may also be used, as *Loopy Cuts* is completely agnostic to how such information are computed. We produce our output meshes by applying one step of midpoint subdivision [Li et al. 1995] to each block of the meta mesh, and optimizing the geometry with edge-cone rectification [Livesu et al. 2015]. Our pipeline runs in minutes; the global running time depends directly on the number of cuts, and indirectly on the complexity of the shape. On average, the generation of the cutting loops takes between 10 and 120 seconds on meshes in the range of 4K-50K tris (often obtained by feature-preserving remeshing from high-resolution meshes); while 3 to 8 seconds per cut were necessary to cut models between 100K and 200K tets.

7 CONCLUSIONS

We present a new approach to block-decomposition for hexahedral meshing. The method combines tracing of strategically placed cross-field coherent cutting surface loops with computation of fair cutting surfaces interpolating one or more such loops. As shown by our results the method outperforms prior work in providing a combination of robustness, feature interpolation, and curvature alignment.

Limitations and Future work. Our framework is not guaranteed to compute a valid decomposition. In particular we envision the following sources of failure. First, our loop formation strategy relies on the underlying cross-field. On surfaces where the cross-field directions change multiple times, the resulting loops may be too complicated or the tracing may not be able to close loops properly, avoiding self-intersections. Second, our cutting surface computation depends on the existence of suitable groups of loops that jointly bound a desired cutting surface. Sometimes, some loops find no mate to pair with, just because such loop cannot be found on the sole basis of the existing line features and the cross field. Finally, our grouping strategy is heuristic and may fail even when suitable loops exist. We did not exploit user interaction at its full potential, since in our current implementation this is allowed only during the pairing and cutting phase; enabling simple user interaction during loop selection may resolve with a few clicks most of the issues described above, for instance by forcing or deviating some loop, or changing the flow of the cross-field. Addressing all the above aspects is an interesting avenue for future research.

ACKNOWLEDGMENTS

This work is partially supported by the EU ERC Advanced Grant CHANGE, grant agreement No.694515.

REFERENCES

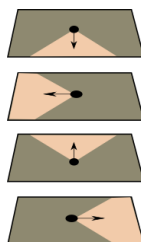
- Ted Blacker. 1996. The Cooper Tool. In *Proc. International Meshing Roundtable*. 13–29.
- Ted Blacker. 2000. Meeting the challenge for automated conformal hexahedral meshing. In *9th international meshing roundtable*. 11–20.
- Ioana Boier-Martin, Holly Rushmeier, and Jingyi Jin. 2004. Parameterization of triangle meshes over quadrilateral domains. In *Proc. Eurographics Symposium on Geometry Processing*. 193–203.
- D. Bommes, H. Zimmer, and L. Kobbelt. 2009. Mixed-integer quadrangulation. *ACM Trans. Graph.* 28, 3 (2009), 77.
- Yuri Boykov and Vladimir Kolmogorov. 2004. An experimental comparison of min-cut/max-flow algorithms for energy minimization in vision. *IEEE transactions on pattern analysis and machine intelligence* 26, 9 (2004), 1124–1137.
- Yuri Boykov, Olga Veksler, and Ramin Zabih. 2001. Fast approximate energy minimization via graph cuts. *IEEE Transactions on pattern analysis and machine intelligence* 23, 11 (2001), 1222–1239.
- Marcel Campen, David Bommes, and Leif Kobbelt. 2012. Dual loops meshing: quality quad layouts on manifolds. *ACM Trans. Graph.* 31, 4 (2012), 110.
- Nathan A. Carr, Jared Hoberock, Keenan Crane, and John C. Hart. 2006. Rectangular Multi-chart Geometry Images. In *Proc. Eurographics Symposium on Geometry Processing*. 181–190.
- Gianmarco Cherchi, Marco Livesu, and Riccardo Scateni. 2016. Polycube Simplification for Coarse Layouts of Surfaces and Volumes. *Computer Graphics Forum* (2016). <https://doi.org/10.1111/cgf.12959>
- Massimiliano Corsini, Paolo Cignoni, and Roberto Scopigno. 2012. Efficient and Flexible Sampling with Blue Noise Properties of Triangular Meshes. *IEEE Transactions on Visualization and Computer Graphics* 18, 6 (June 2012), 914–924. <https://doi.org/10.1109/TVCG.2012.34>
- Joel Daniels II, Claudio T. Silva, and Elaine Cohen. 2009. Semi-regular Quadrilateral-only Remeshing from Simplified Base Domains. *Comput. Graph. Forum* 28, 5 (July 2009), 1427–1435.
- Fernando de Goes, Mathieu Desbrun, and Yiying Tong. 2016. Vector field processing on triangle meshes. In *ACM SIGGRAPH 2016 Courses*. ACM, 27.
- Olga Diamanti, Amir Vaxman, Daniele Panozzo, and Olga Sorkine-Hornung. 2014. Designing N -PolyVector Fields with Complex Polynomials. *Computer Graphics Forum (proceedings of EUROGRAPHICS Symposium on Geometry Processing)* 33, 5 (2014), 1–11.
- Xianzhong Fang, Weiwei Xu, Hujun Bao, and Jin Huang. 2016. All-hex Meshing Using Closed-form Induced Polycube. *ACM Trans. Graph.* 35, 4, Article 124 (July 2016), 9 pages. <https://doi.org/10.1145/2897824.2925957>
- Xiao-Ming Fu, Chong-Yang Bai, and Yang Liu. 2016. Efficient Volumetric PolyCube-Map Construction. In *Computer Graphics Forum*, Vol. 35. Wiley Online Library, 97–106.
- Shuming Gao, Zhihao Zheng, Rui Wang, Yizhou Liao, and Mao Ding. 2018. Dual Surface Based Approach to Block Decomposition of Solid Models. In *Proceedings 27th International Meshing Roundtable*.
- Xifeng Gao, Zhigang Deng, and Guoning Chen. 2015. Hexahedral mesh re-parameterization from aligned base-complex. *ACM Transactions on Graphics (TOG)* 34, 4 (2015), 142.
- Xifeng Gao, Wenzel Jakob, Marco Tarini, and Daniele Panozzo. 2017a. Robust Hex-dominant Mesh Generation Using Field-guided Polyhedral Agglomeration. *ACM Trans. Graph.* 36, 4, Article 114 (July 2017), 13 pages. <https://doi.org/10.1145/3072959.3073676>
- Xifeng Gao, Daniele Panozzo, Wenping Wang, Zhigang Deng, and Guoning Chen. 2017b. Robust structure simplification for hex re-meshing. *ACM Transactions on Graphics (TOG)* 36, 6 (2017), 185.
- James Gregson, Alla Sheffer, and Eugene Zhang. 2011. All-Hex Mesh Generation via Volumetric PolyCube Deformation. *Computer Graphics Forum* 30, 5 (2011), 1407–1416.
- Gaël Guennebaud, Benoît Jacob, et al. 2010. Eigen v3. <http://eigen.tuxfamily.org>. (2010).
- Jin Huang, Tengfei Jiang, Zeyun Shi, Yiying Tong, Hujun Bao, and Mathieu Desbrun. 2014. L1-Based Construction of Polycube Maps from Complex Shapes. *ACM Transactions on Graphics (TOG)* 33, 3 (2014), 25.
- Yasushi Ito, Alan M Shih, and Bharat K Soni. 2009. Octree-based reasonable-quality hexahedral mesh generation using a new set of refinement templates. *Internat. J. Numer. Methods Engrg.* 77, 13 (2009), 1809–1833.
- Wenzel Jakob, Marco Tarini, Daniele Panozzo, and Olga Sorkine-Hornung. 2015. Instant field-aligned meshes. *ACM Trans. Graph.* 34, 6 (2015), 189–1.
- Tengfei Jiang, Jin Huang, Yuanzhen Wang, Yiying Tong, and Hujun Bao. 2014. Frame field singularity correction for automatic hexahedralization. *IEEE Transactions on Visualization and Computer Graphics* 20, 8 (2014), 1189–1199.
- F. Kälberer, M. Nieser, and K. Polthier. 2007. QuadCover: Surface Parameterization using Branched Coverings. *Comput. Graph. Forum* 26, 3 (2007), 375–384.
- Vladimir Kolmogorov and Ramin Zabih. 2004. What energy functions can be minimized via graph cuts? *IEEE Transactions on Pattern Analysis & Machine Intelligence* 2 (2004), 147–159.
- Nicolas Kowalski, Franck Ledoux, and Pascal Frey. 2016. Smoothness driven frame field generation for hexahedral meshing. *Computer-Aided Design* 72 (2016), 65–77.
- Nicolas Kowalski, Franck Ledoux, Matthew L Staten, and Steve J Owen. 2012. Fun sheet matching: towards automatic block decomposition for hexahedral meshes. *Engineering with Computers* 28, 3 (2012), 241–253.
- Michael Kremer, David Bommes, Isaak Lim, and Leif Kobbelt. 2014. *Advanced Automatic Hexahedral Mesh Generation from Surface Quad Meshes*. 147–164.
- Mark Lanthier, Anil Maheshwari, and Jörg-Rüdiger Sack. 2001. Approximating shortest paths on weighted polyhedral surfaces. *Algorithmica* 30, 4 (2001), 527–562.
- Bruno Lévy and Yang Liu. 2010. Lp Centroidal Voronoi Tessellation and its Applications. *ACM Transactions on Graphics (SIGGRAPH conference proceedings)* (2010).
- TS Li, RM McKeag, and CG Armstrong. 1995. Hexahedral meshing using midpoint subdivision and integer programming. *Computer methods in applied mechanics and engineering* 124, 1-2 (1995), 171–193.
- Yufei Li, Yang Liu, Weiwei Xu, Wenping Wang, and Baining Guo. 2012. All-hex Meshing Using Singularity-restricted Field. *ACM Trans. Graph.* 31, 6 (2012).
- Hongwei Lin, Sinan Jin, Hongwei Liao, and Qun Jian. 2015. Quality Guaranteed All-hex Mesh Generation by a Constrained Volume Iterative Fitting Algorithm. *Comput. Aided Des.* 67, C (Oct. 2015), 107–117. <https://doi.org/10.1016/j.cad.2015.05.004>
- Heng Liu, Paul Zhang, Edward Chien, Justin Solomon, and David Bommes. 2018. Singularity-constrained octahedral fields for hexahedral meshing. *ACM Transactions on Graphics (TOG)* 37, 4 (2018), 93.
- Shang-sheng Liu and Rajit Gadh. 1997. Automatic Hexahedral Mesh Generation by Recursive Convex and Swept Volume Decomposition. In *6th International Meshing Roundtable, Sandia National Laboratories*. 217–231.
- Marco Livesu, Marco Attene, Giuseppe Patané, and Michela Spagnuolo. 2017. Explicit Cylindrical Maps for General Tubular Shapes. *Computer-Aided Design* 90 (2017), 27–36. <https://doi.org/10.1016/j.cad.2017.05.002>
- Marco Livesu, Alessandro Muntoni, Enrico Puppo, and Riccardo Scateni. 2016. Skeleton-driven Adaptive Hexahedral Meshing of Tubular Shapes. In *Proceedings of the 24th Pacific Conference on Computer Graphics and Applications (PG '16)*. 237–246.

- Marco Livesu, Alla Sheffer, Nicholas Vining, and Marco Tarini. 2015. Practical Hex-mesh Optimization via Edge-cone Rectification. *ACM Trans. Graph.* 34, 4, Article 141 (July 2015), 11 pages. <https://doi.org/10.1145/2766905>
- Marco Livesu, Nicholas Vining, Alla Sheffer, James Gregson, and Riccardo Scateni. 2013. PolyCut: Monotone Graph-Cuts for PolyCube Base-Complex Construction. *Transactions on Graphics (Proc. SIGGRAPH ASIA 2013)* 32, 6 (2013). <https://doi.org/10.1145/2508363.2508388>
- Loïc Maréchal. 2009. *Advances in Octree-Based All-Hexahedral Mesh Generation: Handling Sharp Features*. Springer Berlin Heidelberg, Berlin, Heidelberg, 65–84. https://doi.org/10.1007/978-3-642-04319-2_5
- Katsuhiro Miyoshi and Ted Blacker. 2000. Hexahedral Mesh Generation Using Multi-Axis Cooper Algorithm. In *Proc. International Meshing Roundtable*. 89–97.
- M. Nieser, U. Reitebuch, and K. Polthier. 2011. CubeCover: A Parameterization of 3D Volumes. *Computer Graphics Forum* 30, 5 (2011), 1397–1406. <https://doi.org/10.1111/j.1467-8659.2011.02014.x>
- Steven Owen. 2009. A Survey of Unstructured Mesh Generation Technology. (2009). <http://www.andrew.cmu.edu/user/sowen/survey/hexsurv.html>
- Daniele Panozzo, Yaron Lipman, Enrico Puppo, and Denis Zorin. 2012. Fields on Symmetric Surfaces. *ACM Trans. Graph.* 31, 4 (July 2012), 111:1–111:12.
- Philippe P. Pébay, David Thompson, Jason Shepherd, Patrick Knupp, Curtis Lisle, Vincent A. Magnotta, and Nicole M. Grosland. 2007. New Applications of the Verdict Library for Standardized Mesh Verification Pre, Post, and End-to-End Processing. In *Proc. International Meshing Roundtable*. 535–552.
- Nico Pietroni, Enrico Puppo, Giorgio Marcias, Roberto Roberto, and Paolo Cignoni. 2016. Tracing Field-Coherent Quad Layouts. *Comput. Graph. Forum* 35, 7 (Oct. 2016), 485–496. <https://doi.org/10.1111/cgf.13045>
- William Roshan Quadros. 2014. LayTracks3D: A New Approach to Meshing General Solids using Medial Axis Transform. *Procedia Engineering* 82 (2014), 72 – 87. <https://doi.org/10.1016/j.proeng.2014.10.374> 23rd International Meshing Roundtable (IMR23).
- Nicolas Ray, Dmitry Sokolov, Maxence Reberol, Franck Ledoux, and Bruno Lévy. 2017. Hexahedral Meshing: Mind the Gap! (2017).
- Eloi Ruiz-Gironés, Xevi Roca, and Josep Sarrate. 2011. Using a computational domain and a three-stage node location procedure for multi-sweeping algorithms. *Advances in Engineering Software* 42, 9 (2011), 700–713.
- R. Schneiders. 1996. A grid-based algorithm for the generation of hexahedral element meshes. *Engineering with Computers* 12, 3 (01 Sep 1996), 168–177. <https://doi.org/10.1007/BF01198732>
- A. Sheffer, M. Etzion, A. Rappoport, and M. Bercovier. 1999. Hexahedral Mesh Generation using the Embedded Voronoi Graph. *Engineering with Computers* 15, 3 (01 Sep 1999), 248–262.
- J. F. Shepherd and C. R. Johnson. 2008. Hexahedral mesh generation constraints. *Eng. with Computers* 24, 3 (2008), 195–213.
- Hang Si. 2015. TetGen, a Delaunay-based quality tetrahedral mesh generator. *ACM Transactions on Mathematical Software (TOMS)* 41, 2 (2015), 11.
- Dmitry Sokolov, Nicolas Ray, Lionel Untereiner, and Bruno Lévy. 2016. Hexahedral-Dominant Meshing. *ACM Trans. Graph.* 35, 5, Article 157 (June 2016), 23 pages. <https://doi.org/10.1145/2930662>
- Justin Solomon, Amir Vaxman, and David Bommes. 2017. Boundary element octahedral fields in volumes. *ACM Transactions on Graphics (TOG)* 36, 3 (2017), 28.
- Matthew L. Staten, Steven J. Owen, and Ted D. Blacker. 2005. Unconstrained Paving & Plastering: A New Idea for All Hexahedral Mesh Generation. In *Proc. International Meshing Roundtable*. 399–416.
- Marco Tarini, Kai Hormann, Paolo Cignoni, and Claudio Montani. 2004. Polycube-maps. In *ACM transactions on graphics (TOG)*, Vol. 23. ACM, 853–860.
- Timothy J Tautges, Ted Blacker, and Scott A Mitchell. 1996. The whisker weaving algorithm: a connectivity-based method for constructing all-hexahedral finite element meshes. *Internat. J. Numer. Methods Engrg.* 39, 19 (1996), 3327–3349.
- Amir Vaxman, Marcel Campen, Olga Diamanti, Daniele Panozzo, David Bommes, Klaus Hildebrandt, and Mirela Ben-Chen. 2016. Directional field synthesis, design, and processing. In *Computer Graphics Forum*, Vol. 35. Wiley Online Library, 545–572.
- Rui Wang, Chun Shen, Jinming Chen, Haiyan Wu, and Shuming Gao. 2017. Sheet operation based block decomposition of solid models for hex meshing. *Computer-Aided Design* 85 (2017), 123 – 137. <https://doi.org/10.1016/j.cad.2016.07.016> 24th International Meshing Roundtable Special Issue: Advances in Mesh Generation.

A COMPUTING CUTTING LOOPS

A.1 Field-coherent loops

Following [Kälberer et al. 2007], the four components of a cross field X can be separated on a stratification \mathcal{M}_4 of manifold \mathcal{M} into four sheets, defined as follows (inset). For every



point p of \mathcal{M} , except the singularities of X , consider four copies $p_0, p_{\frac{\pi}{2}}, p_{\pi}$ and $p_{\frac{3\pi}{2}}$, each consisting of p together with one of the four directions of X at p , such that $p_0 = -p_{\pi}$ and $p_{\frac{\pi}{2}} = -p_{\frac{3\pi}{2}}$. We call each such copy p_{θ} of p a *point-arrow* meaning that it incorporates both a position on \mathcal{M} and a direction on its tangent space. Space \mathcal{M}_4 consists of four sheets, each corresponding to \mathcal{M} less the singularities of X , such that the point-arrows p_{θ} defined above are distributed among the layers to form a smooth direction field (see inset). Generally speaking, if X has singularities, the direction field on \mathcal{M}_4 turns about such singularities, thus sliding between different sheets, and \mathcal{M}_4 consists of a single connected component. Space \mathcal{M}_2 is the quotient space of \mathcal{M}_4 obtained by identifying pairs of point-arrows p_{θ} and $-p_{\theta}$, thus consisting of two sheets, each endowing a line field. Manifold \mathcal{M} can be also seen as a quotient space of \mathcal{M}_4 , by identifying the four point-arrows at each point p .

Following [Pietroni et al. 2016], a smooth (oriented) curve ℓ on \mathcal{M}_4 is said to be a *field-coherent* path if its tangent direction at all points does not differ for more than $\pi/4$ from the underlying direction field on \mathcal{M}_4 (pink wedges in the inset). With abuse of notation, we denote by ℓ also the corresponding curves on \mathcal{M}_2 and \mathcal{M} , regarded as quotient spaces of \mathcal{M}_4 . Two field-coherent paths ℓ_1 and ℓ_2 are said to intersect *tangentially* if they intersect in \mathcal{M}_2 ; while they intersect *orthogonally* if they intersect in \mathcal{M} but they do not intersect in \mathcal{M}_2 .

The drift of a field-coherent path w.r.t. X comes from the angle between the direction field and the tangent of ℓ at each point along it. Following [Pietroni et al. 2016] we adopt an anisotropic metric on \mathcal{M}_4 that increases the length of a path proportionally to its amount of drift:

$$\|w\|_X = |w| \left(1 + \alpha \frac{\angle(p_{\theta}, w)}{\pi/4}\right) \quad (3)$$

where w is a tangent vector at p , $|w|$ is its Euclidean norm, p_{θ} is the reference direction on \mathcal{M}_4 , \angle measures the unsigned angle between a pair of vectors, and α is a parameter that tunes the amount of penalty for the drift. A field-coherent *geodesic* path between two point-arrows on \mathcal{M}_4 is a field-coherent path joining them that is shortest according to the above metric. We define a *field-coherent geodesic loop* to be a non-null field-coherent geodesic path that starts and ends at the same point.

A.2 Extending features to loops

In order to force loops to run along line features, we modify the graph \mathcal{G} as follows:

- Given a line feature f , we create two *corridors*, each made of a strip of triangles of \mathcal{M} incident at f , one for each side of f (see Figure 20.a);
- For each face in a corridor, we consider all Steiner nodes of \mathcal{G} that are coherent with the direction of f and that lie on edges crossing the corridor (see Figure 20.b);
- We reduce the weight of arcs connecting pairs of such nodes in the corridor (green arcs in Figure 20.c);

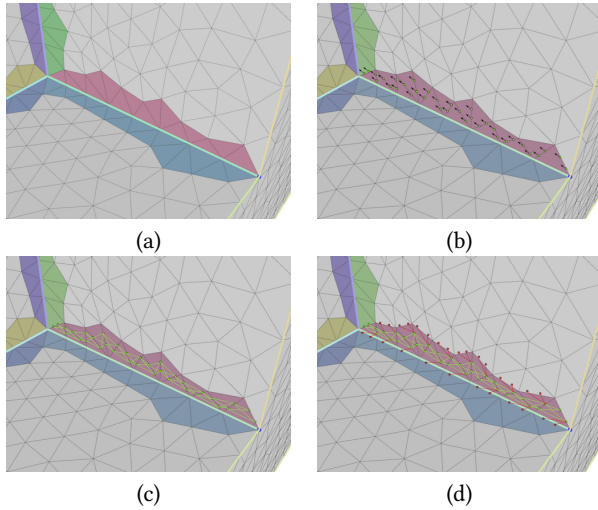


Fig. 20. Tracing loops along curve features requires modifying the graph \mathcal{G} to avoid the endpoint singularities: we consider the triangles on one side of a curve feature (a), we choose the Steiner points of \mathcal{G} of that side (b) and we weight to zero the red arcs inside the corridor (c), and inhibit the green arcs exiting from the corridor (d).

- We inhibit all arcs that connect such nodes with nodes at the boundary of the corridor (red arcs in Figure 20.d).

For each line feature f , we create one seed node per side of f and we trace a set of candidate loops from all such nodes. Note that, in the modified graph, each path that enters a corridor is forced to traverse it totally, and paths traversing several corridors (i.e., joining or bridging different line features) are favoured because of their reduced cost (see Figure 6.a). Note that each feature may be traversed by multiple loops in the set of candidates. In the process of generating the loops that extends line features we select loops in a greedy manner, preferring the ones that span the largest length of open features.

B MODEL CUTTING

B.1 Similarity metrics for loop pairing

We formalize here the similarity metrics for planes and cylinders used to perform loop pairing. Both metrics are defined as penalty metrics in the range $(0, 1]$, meaning that lower values denote higher similarity. Given two loops ℓ_i, ℓ_j of type I, II that are centered at c_i, c_j and span two planes with normals n_i, n_j , respectively, we define their plane similarity as follows

$$E_{\text{plane}} = \frac{1}{2} \left(\exp \left(\frac{-|n_i \cdot n_j|^2}{0.2} \right) + \exp \left(\frac{-(1 - \max(|c \cdot n_i|, |c \cdot n_j|))^2}{0.2} \right) \right).$$

The first term weighs angle similarity between plane normals; the second term weighs the maximum distance between the centroid of ℓ_i and the plane spanned by ℓ_j , and vice versa. Vector c is defined as $(c_i - c_j) / \|c_i - c_j\|$.

Given two loops ℓ_i, ℓ_j of type III, that are centered at c_i, c_j , have radius r_i, r_j and span two oriented lines d_i, d_j , respectively, we

define their cylinder similarity as follows

$$E_{\text{cyl}} = \frac{1}{2} \left(1 - \exp \left(\frac{-(1 + d_i \cdot d_j)^2}{0.2} \right) + \min \left(\frac{r_i}{r_j}, \frac{r_j}{r_i} \right) \right).$$

The first term measures angle similarity, and promotes pairing between loops laid on oppositely oriented surfaces. The second term matches the radii of the cylinders, and serves to find the best geometric matching in presence of concentric loops.

B.2 Backup pairing strategy

The backup pairing strategy is used when the geometric loop pairing does not provide a globally consistent bi-partition of \mathcal{M} . It computes a bi-partition that assigns to each triangle in the mesh either 0 or 1, and minimizes the total length of the edges having opposite labels at their sides

$$\min \sum_{e \in \mathcal{M}} C_e(l_i, l_j)$$

where e are the mesh edges, l_i, l_j are the labels associated to the triangles incident at it, and the per edge cost energy C_e is defined as

$$C_e(l_i, l_j) = \begin{cases} 0 & \text{if } l_i = l_j \\ |e| & \text{if } l_i \neq l_j \end{cases}$$

We compute the solution using the min-cut implementation provided by [Boykov and Kolmogorov 2004; Boykov et al. 2001; Kolmogorov and Zabih 2004]. To guarantee that the initial cut is used to bi-partition, we set boundary conditions that impose that the triangles at its two sides must receive opposite labels.

B.3 Topological cleaning

Since the final meta-mesh reveals itself cut after cut (Figure 12), extracting it when none or just a few cuts have been performed may result in a number of topological inconsistencies that affect its cells, such as: dangling edges, islands, non-manifold vertices and faces with less than two vertices (Figure 21). We make the extraction of the meta-mesh robust against all these defects by using a set of topological operators that collapse all the topologically illegal entities, as depicted in the bottom line of the figure.

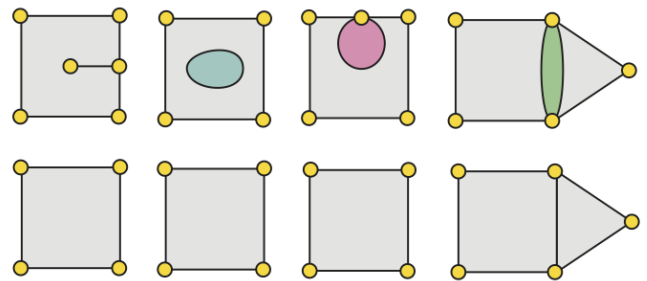


Fig. 21. Extracting the meta-mesh at early stages of the algorithm may result in cells having a number of topological artifacts, such as: dangling edges (left); islands (middle-left); non manifold vertices (middle-right); and faces having less than three vertices (right). We address such cases during mesh extraction, ignoring topological inconsistencies and collapsing non valid faces (bottom).